Bland T, Tong J, Ward B, Parker NG.

Geometric distortion of area in medical ultrasound images.

***Journal of Physics Conference Series* 2017, 797, 012002.**

DOI link to article:

http://dx.doi.org/10.1088/1742-6596/797/1/012002

Date deposited:

27/01/2017

Geometric distortion of area in medical ultrasound images

2017 J. Phys.: Conf. Ser. 797 012002

(http://iopscience.iop.org/1742-6596/797/1/012002)

IOP Conf. Series: Journal of Physics: Conf. Series **797** (2017) 012002 doi:10.1088/1742-6596/797/1/012002

Geometric distortion of area in medical ultrasound images

T Bland[1], J Tong[2], B Ward[2] and N G Parker[1]

[1] School of Mathematics and Statistics, Newcastle University, Newcastle upon Tyne, UK
[2] Regional Medical Physics Department, Freeman Hospital, Newcastle upon Tyne, UK

E-mail: nick.parker@ncl.ac.uk

Abstract. Medical ultrasound scanners are typically calibrated to a speed of sound corresponding to the soft tissue average of 1540 m s^{-1}. In regions of different sound speed, for example, organs and tumours, the B-mode image becomes geometrically distorted from the true tissue cross-section, due to refraction and the misrepresentation of length. A ray model is developed to predict this distortion for a generalized two-dimensional object with atypical speed of sound, and verified against ultrasound images of a test object. We quantify the areal image distortion as a function of the key dependencies, including the speed of sound mismatch, the scanning format, the object size and its elongation. Our findings show that the distortion of area can be significant, even for relatively small speed of sound mismatches. For example, a 5% speed mismatch typically leads to a $10-20\%$ distortion in area. These findings have implications for the accuracy of ultrasound-based evaluation of area and volume.

1. Introduction

Medical ultrasound scanners conventionally assume a uniform speed of sound throughout the body, corresponding to the soft tissue average of 1540 m s^{-1} [1]. However, bodily soft tissue is acoustically inhomogeneous and its speed of sound can vary by several percent across different regions [2], e.g., typical speeds of sound in fat, muscle and liver are 1440, 1580 and 1590 m s^{-1}, respectively [3]. These variations in speed of sound are detrimental to the image formation and the accuracy of its representation of the true tissue profile. For example, they induce aberrations in the acoustic wavefront, which degrades the formation and steering of the ultrasonic beam, and in turn reduces the spatial and contrast resolution of the image [4, 5, 6]; the correction of these aberrations is an active area of research (see, for example, [7, 8, 9, 10, 11]). Another implication of such speed variations is that the scanner overlooks refraction of the beam and misregisters the beam path length; this introduces geometric distortions into the image whereby the position of certain echoes will deviate from the actual locations of the features which generated them. While the presence of these geometric distortions is well known within the ultrasound community [12, 13, 14, 15, 16, 18, 19], they are usually deemed negligible for the purposes of qualitative diagnostics. However, there is increasing use of ultrasound imaging for quantitative measurements, notably the rapid developments in ultrasound-based evaluation of the volume of organs and tumours [20, 21, 22]. These geometric distortions introduce systematic errors in such measurements and are a key limiting factor in their diagnostic accuracy [2, 23], and yet this distortion remains largely unexplored as a source of error in area and volume measurements.

To illustrate this effect, consider an ambient medium with speed of sound v_1 and an ultrasound scanner which assumes the same value. An object with atypical speed of sound $v_2 \neq v_1$ is embedded within the medium and a B-mode image taken of its cross-section. Then, the distance within the object will be misrepresented in the image and the refraction at the object boundary will not be accounted for, both of which will contribute to the geometric distortion of the object's image. While this distortion has been predicted previously [13, 14, 15, 16, 18, 17, 19], a quantitative understanding remains lacking. This work aims to address this issue by quantifying the distortion of area of generalized objects in two-dimensional B-mode images. This is a first step in understanding the distortion of volume in 3D ultrasound images, which are typically reconstructed from 2D images [33, 34, 35]; then, if the object in question has atypical speed of sound, the above 2D distortion will introduce errors in the calculated area of each scanning plane, and thus the total calculated volume.

A ray model (described in Section 2) forms the basis of our work. Despite its simplicity, it is well-suited to reveal the underlying mapping of the object boundary to its image, the main focus of this work. Our work may be considered as an extension to that of Ref. [36], which employed a similar methodology to model how points (rather than objects) become geometrically distorted due to an atypical ambient speed of sound. We develop our model across the most common medical transducer arrays: linear, curved, phased, and vector arrays (following the categorization of Ref. [36]). Comparison to ultrasound images of phantoms (Section 3) confirm the success of the ray model in predicting the shape of the image. We quantify the distortion as a function of the speed of sound ratio v_2/v_1, the object's shape and size, and the array type. Our results show that a small speed of sound mismatch can lead to significant distortions: for example, a 5% mismatch in the speeds of sound can lead to around 15% error in the area of a circular object, and this is sensitive to the size and shape of the object. We conclude by discussing the wider implications of our findings within the context of diagnostic evaluation of area and volume.

2. Theory

2.1. Ray Model

We consider an elliptical (two-dimensional) object in the x-z plane, with uniform speed of sound v_2, embedded in an ambient medium with uniform speed of sound v_1. The object has semi-widths b and c. The set-up is depicted in figure 1(a). The scanner is calibrated to a speed of sound denoted v_0, which we assume to correspond to the ambient speed of sound v_1 (in Appendix A we present a more general theory where this is not assumed). We develop the ray model for the curved transducer array; later, we will generalize to other common array types. Beam lines can be considered to spread out from a virtual source (the origin) within the transducer, emanating normal to the transducer surface [36]. The object boundary is represented by the elliptical line $z_{\mathrm{ob}}(x)$ which satisfies the relation

$$\frac{x^2}{b^2} + \frac{\left(z_{\mathrm{ob}} - c - d - d_0\right)^2}{c^2} = 1. \tag{1}$$

where d is the axial distance between the front faces of the object and the transducer, and d_0 is the distance from the virtual source to the transducer surface.

We model the distortion of the object by treating the beam lines as rays. This approximation is valid in the far-field of the source and for objects much larger than the acoustic wavelength. A ray emitted from the transducer surface at point A with coordinates $(x_{\mathrm{A}}, z_{\mathrm{A}})$ is incident on the front face of the object at point B, $(x_{\mathrm{B}}, z_{\mathrm{B}})$, as illustrated in figure 1. This follows the straight line path $z_{\mathrm{AB}}(x) = x \cot\theta_{\mathrm{A}} = (z_{\mathrm{B}}/x_{\mathrm{B}})x$, where $\theta_{\mathrm{A}} = \arctan(x_{\mathrm{B}}/z_{\mathrm{B}})$ is the angle of the emitted ray relative to the vertical. At B, the angle between the normal of the boundary and

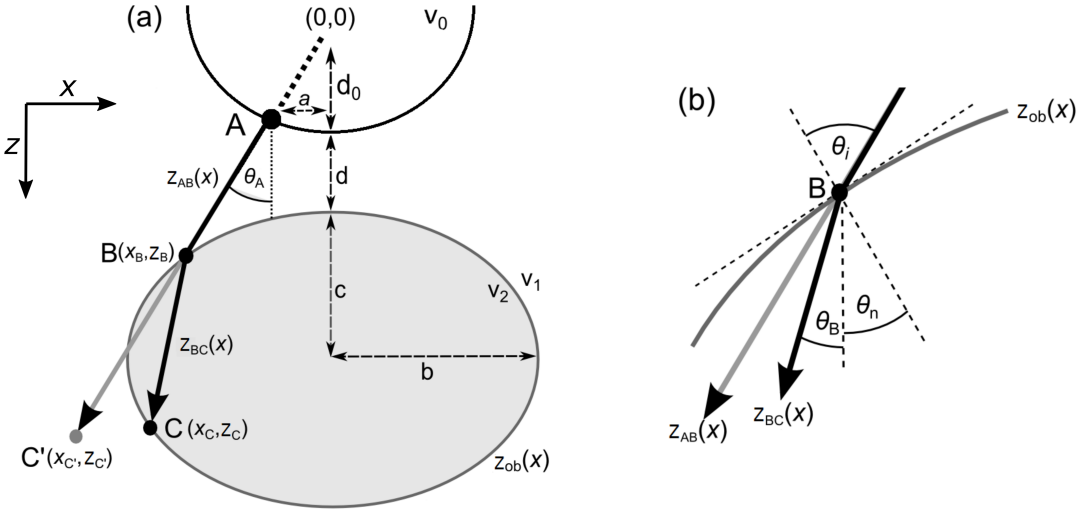

Figure 1. (a) Schematic of the curved transducer array (depicted by the semi-circle at the top of the figure) and elliptical object (speed of sound v_2), embedded within an ambient medium (speed of sound v_1). The ray is emitted from the transducer surface (at point A) at an angle θ_A to the vertical, and is incident at the object surface at point B. For $v_2 \neq v_1$, refraction and misrepresentation of length within the object cause a point C on the far boundary to appear at C'. (b) A close-up of the real ray (black) and image ray (grey) at the point B. The ray is incident on the surface at an angle θ_i to the normal, and the transmitted ray emerges at an angle θ_B to the vertical (with the vertical being at an angle θ_n to the surface normal).

the vertical, θ_n, can be calculated from the gradient of the boundary at B via

$$\tan\theta_\mathrm{n} = \left.\frac{\mathrm{d}z_\mathrm{ob}}{\mathrm{d}x}\right|_{(x_\mathrm{B},z_\mathrm{B})} = \frac{c^2 x_\mathrm{B}}{b^2(d+d_0+c-z_\mathrm{B})}. \tag{2}$$

The angle of incidence at B (relative to the normal) is then $\theta_\mathrm{i} = \theta_\mathrm{n} + \theta_\mathrm{A}$.

At the front face, a component of the wave will be back-scattered to the transducer, registering the presence of this point in the image. Since this ray travels only through the ambient medium, for which the scanner is assumed to be calibrated, the image of this point corresponds to its real location. Of more interest to us is the component of the wave which is refracted through the boundary (the components of the wave that undergo specular reflection or scattering away from the transducer are not registered by the transducer and so we ignore them). This ray is incident on the object's back face at point C, with coordinates $(x_\mathrm{C}, z_\mathrm{C})$, and represented by the straight line $z_\mathrm{BC}(x)$,

$$z_\mathrm{BC}(x) = (x - x_\mathrm{B})\cot\theta_\mathrm{B} + z_\mathrm{B}. \tag{3}$$

θ_B is the angle from the vertical direction, given by $\theta_\mathrm{B} = \theta_\mathrm{r} - \theta_\mathrm{n}$, where θ_r is the angle of refraction. To obtain an expression for θ_r, we rearrange Snell's law, $\sin\theta_\mathrm{i}/\sin\theta_\mathrm{r} = v_1/v_2$, to give

$$\theta_\mathrm{r} = \arcsin\left[\frac{v_2}{v_1}\sin(\theta_\mathrm{A}+\theta_\mathrm{n})\right]. \tag{4}$$

To establish $(x_\mathrm{C}, z_\mathrm{C})$, we seek the intersections of the refracted ray $z_\mathrm{BC}(x)$ with the boundary $z_\mathrm{ob}(x)$. Rearranging equation (3) for x and inserting into equation (1) gives the relation

$$\frac{[(z-z_\mathrm{B})\tan\theta_\mathrm{B} + x_\mathrm{B}]^2}{b^2} + \frac{[z-c-d-d_0]^2}{c^2} = 1. \tag{5}$$

Multiplying this out leads to a quadratic equation in z and thus two solutions for z. The larger of these corresponds to point C (and the smaller to point B). Hence we obtain the z-coordinate of C to be

$$z_{\rm C} = z_{\rm B} + 2\left\{\left[\frac{c^2 x_{\rm B}\tan\theta_{\rm B} - b^2 d' - z_{\rm B}c^2\tan^2\theta_{\rm B}}{c^2\tan^2\theta_{\rm B}+b^2}\right]^2 + \frac{c^2b^2 - b^2d'^2 - c^2\left[x_{\rm B}-z_{\rm B}\tan\theta_{\rm B}\right]^2}{c^2\tan^2\theta_{\rm B}+b^2}\right\}^{1/2} \quad (6)$$

where $d' = d + d_0 + c$. $x_{\rm C}$ then follows from equation (1).

Having established the path to C, we proceed to locate its image, C'. The paths AB and BC have lengths $L_{\rm AB} = \sqrt{x_{\rm B}^2 + z_{\rm B}^2}$ and $L_{\rm BC} = \sqrt{(x_{\rm C}-x_{\rm B})^2 + (z_{\rm C}-z_{\rm B})^2}$, respectively. Assuming that the ray returns to the transducer along the same path, the total travel time is

$$t = \frac{2L_{\rm AB}}{v_1} + \frac{2L_{\rm BC}}{v_2}. \quad (7)$$

The transducer, calibrated to the ambient speed of sound v_1, perceives the ray as the unrefracted path, i.e. along $z_{\rm AB}(x)$, with the same travel time t. Hence the path AC' has length

$$L_{\rm AC'} = \frac{v_1 t}{2} = L_{\rm AB} + \frac{v_1}{v_2}L_{\rm BC}. \quad (8)$$

The position of C' then follows as

$$(x_{\rm C'}, z_{\rm C'}) = (L_{\rm AC'}\sin\theta_{\rm A}, L_{\rm AC'}\cos\theta_{\rm A}). \quad (9)$$

For $v_1 \neq v_2$ the image point differs from the real point, partly due to refraction of the ray at the near face of the object, and secondly due to the rescaling of length due to the speed of sound misrepresentation. For $v_2 < v_1$, the image is extended from the transducer (due to the longer travel time within the object), while for $v_2 > v_1$ the image is moved closer to the transducer (due to the shorter travel time within the object).

2.2. Generalization to Other Array Types

There are 3 other main types of multielement transducer currently in use in medical imaging: the linear, phased, and vector arrays. The ray structure for these array types can be found elsewhere [36]. Below we summarize how the ray model can be extended to these types.

Vector array: In this array, beam lines spread out from a virtual source located within the (flat) transducer. Since we assume that $v_0 = v_1$ (i.e. the scanner calibrated speed of sound equals the ambient speed of sound), no virtual refraction takes place at the transducer surface, and so the only modification is in the position at which the ray emerges from the surface, accounted for in the model by the coordinates $(x_{\rm A}, z_{\rm A})$.

Phased array: In a phased array beam lines spread out from a virtual source at the surface of the transducer, accounted for by setting $d_0 = 0$.

Linear array: In a linear array, beam lines emerge from the transducer surface, i.e. $d_0 = 0$, normal to the transducer face, i.e. $\theta_{\rm A} = 0$. Note that the image position (9) then reduces to

$$(x_{\rm C'}, z_{\rm C'}) = (0, L_{\rm AC'}), \quad (10)$$

i.e. the image point appears directly above the source.

2.3. Area Evaluation

The image boundary will, in general, be irregularly-shaped. To evaluate the enclosed area we exploit Green's theorem [37]. Green's theorem states that, for a region R bound by a simple closed path Γ, then,

$$\iint_R \left(\frac{\partial v}{\partial x} - \frac{\partial u}{\partial z} \right) \mathrm{d}x \, \mathrm{d}z = \oint_\Gamma \{ u \, \mathrm{d}x + v \, \mathrm{d}z \} , \tag{11}$$

where $u(x, z)$ and $v(x, z)$ are arbitrary functions, and the path of integration along Γ is taken to be counter-clockwise. Taking the choice of functions $u(x, z) = -z/2$ and $v(x, z) = x/2$ then the left-hand side of equation (11) reduces to $\iint_R \mathrm{d}x \, \mathrm{d}z$, which corresponds to the area of the region R. It then follows that we can express the area A of this region via a line integral around its boundary Γ via

$$\mathrm{A} = \frac{1}{2} \oint_\Gamma \left(-z \, \mathrm{d}x + x \, \mathrm{d}z \right) . \tag{12}$$

We numerically implement this line integral around the image boundary (discretized as a series of points) to obtain the image area. We quantify the image distortion through the *area distortion* $A_\mathrm{i}/A_\mathrm{r}$, where A_i and A_r are the areas of the image and object. Where discontinuities arise in the image boundary, for the purposes of area evaluation, a straight line traversing the discontinuity is assumed.

3. Materials and Methods

We experimentally analyse the case of a circular object as follows. A hollow spherical aluminium bauble, filled with "liquid 2" and sealed with a latex condom, was suspended (by a wire frame) in a bath of "liquid 1". Its central circular cross-section was imaged from above by an ultrasound scanner (Philips HDI 5000) and curved array (Philips C5-2 40R, operating frequency range 2-5 MHz, $d_0 = 40$ mm). The set-up is depicted in figure 2(a). The transducer is aligned manually with the equator of the object. The overall object radius r was measured with callipers as $r = (3.99 \pm 0.01)$ cm and the transducer-object distance d determined using the scanner's electronic callipers. Where the ambient liquid has the same speed of sound as that assumed by the scanner, this electronic caliper measurement should not suffer any length distortion; where it has a different speed of sound, the electronic caliper measurement is rescaled by a factor v_1/v_0 to account for this distortion. The experiments were run at ambient temperature and the precise bath temperature recorded by digital thermometer.

The aluminium composition of the object was convenient as the high acoustic impedance of aluminium ($\approx$ 17 MRayl) leads to a high contrast image. The aluminium is approximately 1mm thick. At the operating frequency of the scanner probe (2-5 MHz), the wavelength in aluminium is in the range 1-2 mm, and so surface and plate waves can be expected to be highly suppressed. The condom and aluminium shell are sufficiently thin to have negligible impact on our analysis.

For the liquids we employed pure water, pure methanol and an ethanol-water mixture (with 7.25% w/w ethanol). These have room temperature speeds of sound of 1482 m s^{-1} [38], 1100 m s^{-1} [39] and 1540 m s^{-1} [40], respectively (the latter being matched to the tissue average and scanner-assumed value). Note that, while the methanol case of 1100 m s^{-1} is not a clinically relevant speed of sound, for this work it provides a more extreme value with which to further test our ray model. The bath temperature varied in the range 18-23°C and we corrected the speeds of sound used in the model using the established temperature-speed relations [38, 39, 40].

As an initial validation we filled both the object and bath with ethanol-water mixture, such that the system has uniform speed of sound throughout, $v_2 = v_1 = 1540$ m s^{-1}. The B-mode,

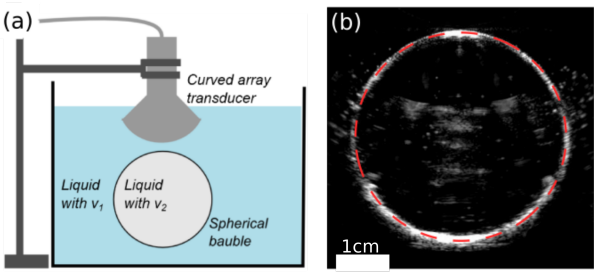

Figure 2. (a) Illustration of the experimental set-up. A curved array transducer, clamped in place, images (from above) the central cross-section of a spherical bauble (diameter 4cm). The bauble is filled with liquid of speed of sound v_2, and the ambient speed of sound is v_1. (b) Corresponding B-mode image for $v_2 = v_1 = 1540$ m s^{-1}, both matched to the scanner. The expected object boundary is shown by the dashed red line.

shown in figure 2(b), shows a circular image boundary, confirming that there is no significant geometric distortion, and matches well to the expected circular shape of the object (red dashed line). Indeed, the experimental boundary (defined as the centre/maximum in the echo) deviates by no more than 1mm from the true object boundary. Note the intensity distortion around the boundary: the poles of the object are brightest as a result of specular reflection.

The area of the object image is estimated using the scanner's built-in "lasso" function. This involves the operator specifying several points around the object boundary (defined as the position of the maximum echo from the boundary) by hand; the scanner then returns the area of the defined region.

Three variations of this system were considered.

$v_2 < v_1$**:** Taking ethanol-water mixture as liquid 1 and pure water as liquid 2 embodies a system with $v_2 < v_1$ ($v_2 \approx 0.96 v_1$).

$v_2 \ll v_1$**:** Taking the ethanol-water mixture as liquid 1 and now methanol as liquid 2 embodies a system with $v_2 \ll v_1$ ($v_2 \approx 0.71 v_1$).

$v_2 > v_1$**:** Taking pure water as liquid 1 and the ethanol-water mixture as liquid 2 creates a system with $v_2 > v_1$ ($v_2 \approx 1.04 v_1$).

Note that, for the first two cases, the speed of sound of the ambient liquid is matched to that assumed by the scanner, as per the assumptions of our ray model. This is not true for the third case, and so the ray model must be extended to account for the distortion of the near-face of the object; this is outlined in Appendix A.

4. Results: Circular Objects

We begin by using the ray model to map out the area distortion of circular objects, first for a simplest case of a linear array and then for our primary case of a curved array. The latter will be validated against experimental images. Unless otherwise stated, we assume the nominal parameters $r = 4$ and $d = 2$. Note that length is subsequently presented in arbitrary units.

4.1. Linear Array

In figure 3(a) we show the ray model prediction for $v_2/v_1 = 0.95$; the typical ray behaviour is illustrated by three sets of rays. The rays propagate vertically downwards from the transducer surface (the x-axis, $z = 0$), impinging the near-face (the upper half) of the object boundary. Our assumption that the scanner is matched to the ambient speed of sound means that the

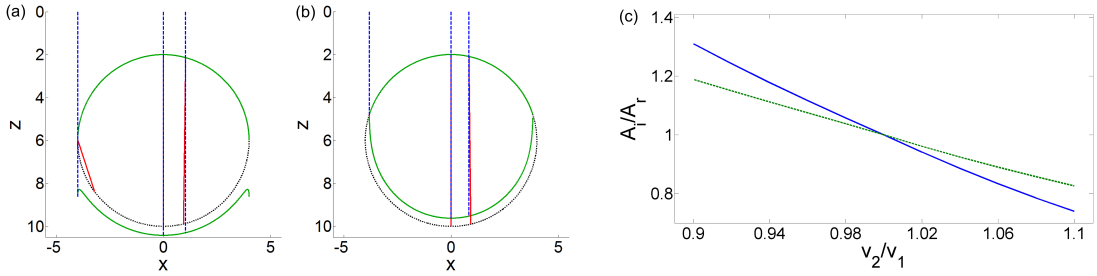

Figure 3. (a) Image (solid green line) of a circular object (dotted black line) with $v_2 = 0.95v_1$ based on a linear array. Three example sets of real rays (dashed blue lines) and their corresponding image rays (solid red lines) are overlaid. (b) Same as above but for $v_2 = 1.05v_1$. (c) Area distortion $A_\mathrm{i}/A_\mathrm{r}$ as a function of the speed of sound ratio v_2/v_1, for the linear array (green dashed line) and curved array (blue solid line). The curved array case will be further detailed in figure 4.

near face is undistorted, that is, the image boundary (solid green line) and the object boundary (dotted black line) overlap here.

At the near-face the real rays (red lines) are refracted inwards; the exception is the central ray which continues vertically due to its zero angle of incidence, θ_i. These rays travel slower within the object since $v_2 < v_1$. The image rays (dashed blue lines) deviate in two ways: they are unrefracted at the near-face, and they appear elongated within the object. The latter effect is best resolved along $x = 0$: here the image ray is simply extended by a distance $2r(v_1/v_2 - 1) \approx 0.42$. Off-axis, the rays are refracted inwards (towards the normal), with the refraction being small across most of the object since θ_i is small (with the deviation being hard to see by eye). Towards the equator of the object, however, θ_i grows rapidly, causing a significant increase in refraction and the real-ray path length in the object. This has two notable effects as $x \to \pm r$: firstly, the increasing inwards refraction leads to the appearance of a gap in the image boundary, and secondly, the divergence of the internal path length leads to the formation of prominent "flicks" in the image boundary [14].

Now consider the case $v_2/v_1 = 1.05$, shown in figure 3(b). Since $v_2 > v_1$ the real rays travel faster than the image rays within the object, and so the far image boundary becomes shifted towards the transducer. Also, the real rays become refracted outwards (away from the normal). This removes the appearance of the above flicks for $x \approx \pm r$. The image boundary again features a gap, although its origin is different to that above: here it is caused when the rays impinge the near face at a sufficiently large angle of incidence that they undergo total internal reflection, and so do not reach the far face.

For the above cases the area distortion is $A_\mathrm{i}/A_\mathrm{r} = 1.093$ and 0.907, respectively. In other words, a 5% speed of sound difference has led to $\approx 10\%$ error in the area. We have also explored the wider dependencies of the area distortion on the key parameters. The area distortion scales approximately linearly with v_2/v_1, as shown in figure 3(c). As d, the transducer-object distance, is varied, the image area A_i is unaffected, since all rays approach the object in the same direction. Moreover, the image area scales in proportion to the size of the circular object, such that the area distortion ratio $A_\mathrm{i}/A_\mathrm{r}$ is independent of r, the radius of the object.

4.2. Curved Array

The corresponding images for a curved array are shown in figure 4(a-b). We see similar qualitative effects as for the linear array: the shifting of the image boundary in front/behind the object boundary, gaps in the image boundary, and the appearance of flicks for $v_2 < v_1$.

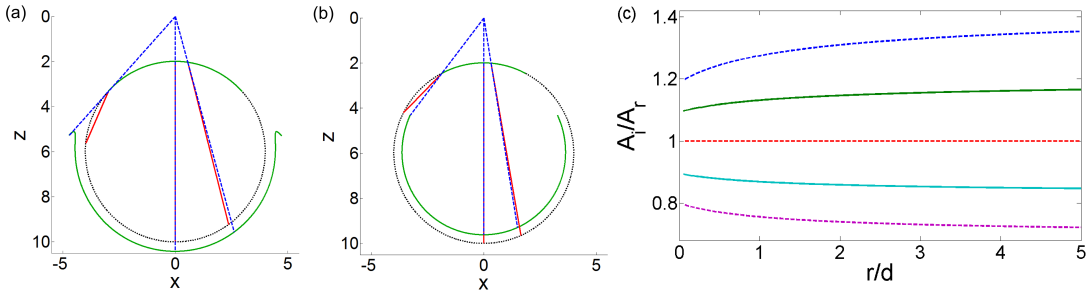

Figure 4. (a)-(b) As figure 3 for a curved array (with $d + d_0 = 2$). (c) Area distortion A_i/A_r of the circular object under curved array imaging as a function of the ratio r/d (recall, r is the object radius and d the distance from the object near-surface to the transducer). Various values of v_2/v_1 are considered ranging from 0.9 (top line) to 1.1 (lowest line) in steps of 0.05. The values $v_2/v_1 = 0.95$ and 1.05 are highlighted by solid lines.

However, the ray structure and image shape are modified further due to the angular spread of the emitted rays. The near-face of the object has reduced extent, such that a greater proportion of the boundary is distorted. The incident rays now approach the tangent of the object fore of the equator, which causes a corresponding shift in the gaps and flicks in the boundary towards the transducer. For the $v_2 < v_1$ case we find $A_i/A_r = 1.147$; for $v_2 > v_1$ we find $A_i/A_r = 0.859$. In other words, a 5% difference in sound speeds for the curved array leads to over 14% deviation in area.

As for the linear array, the variation of the area distortion with v_2/v_1 is approximately linear [figure 3(c)], but with greater deviation than for the linear array. The dependence on r and d is more complicated for the curved array since these parameters control the angular spread of the incident rays. Figure 4(c) shows that the change in area distortion (relative to the undistorted value $A_i/A_r = 1$) increases with r/d; this is due to the increasing angular spread of rays as r/d increases, leading to greater refractive effects and increasing the proportion of the boundary which is distorted.

4.3. Experimental Validation

Experimental B-mode images (with curved array) of the circular test object are shown in figure 5(i), alongside (ii) the ray model predictions of the distorted boundary, for following 3 speed of sound scenarios.

(a) $v_2 < v_1$: Here we consider $v_1 = 1540$ m s^{-1} (ethanol-water mixture) and $v_2 = 1490$ m s^{-1} (water), giving $v_2/v_1 = 0.96$. No geometric distortion is evident at the near face but the far face is shifted away from the transducer, in good agreement with the ray model (dashed green line). The predicted area distortion is $A_i/A_r = 1.076$. The scanner area estimate is $A_i/A_r = 1.074$, in good agreement with the theoretical result.

(b) $v_2 \ll v_1$: Now taking $v_2 = 1100$ m s^{-1} (methanol) gives the more extreme case of $v_2/v_1 = 0.71$. The far-face of the image is highly distorted, in good agreement with the ray model. The theoretical area distortion is $A_i/A_r = 1.97$ (i.e. the image has approximately twice the area of the object), close to the scanner estimate $A_i/A_r = 2.02$.

(c) $v_2 > v_1$: Lastly, we take $v_1 = 1490$ m s^{-1} (water) and $v_2 = 1540$ m s^{-1} (ethanol-water mixture), giving $v_2/v_1 = 1.04$. The ambient liquid is no longer matched to the scanner calibration, causing the near face to become slightly shifted *towards* the far face. Again, the overall image shape agrees well with the ray model (in this case based on the extended

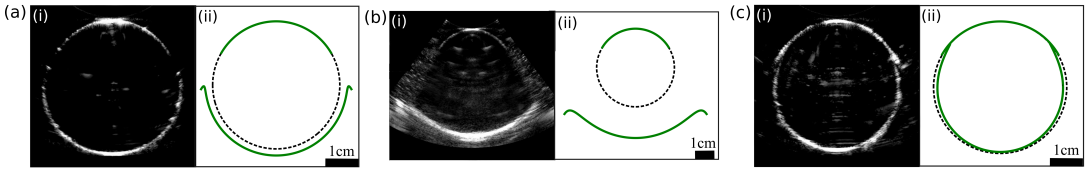

Figure 5. (i) B-mode images of the circular object of speed v_2 (imaged from above in a liquid with speed v_1), for various speed of sound combinations, with (ii) the corresponding ray model prediction of the image boundary (green lines). In (ii) the object boundary is also shown (black dashed line). (a) $v_2 = 1490$ m s^{-1} and $v_1 = 1540$ m s^{-1}, giving $v_2/v_1 = 0.968$. (b) $v_2 = 1100$ m s^{-1} and $v_1 = 1540$ m s^{-1}, giving $v_2/v_1 = 0.71$. (c) $v_1 = 1490$ m s^{-1} and $v_2 = 1540$ m s^{-1}, giving $v_2/v_1 = 1.034$.

theory in Appendix A). The theoretical area distortion $A_\mathrm{i}/A_\mathrm{r} = 0.945$ is close to the scanner estimate $A_\mathrm{i}/A_\mathrm{r} = 0.966$.

These results validate the use of the ray model in predicting the geometric distortion of the object boundary.

5. Results: Elliptical Objects

We extend our theoretical analysis to the more general case of elliptical objects, which allows us to explore the effect of elongation. For brevity, we focus on the curved array.

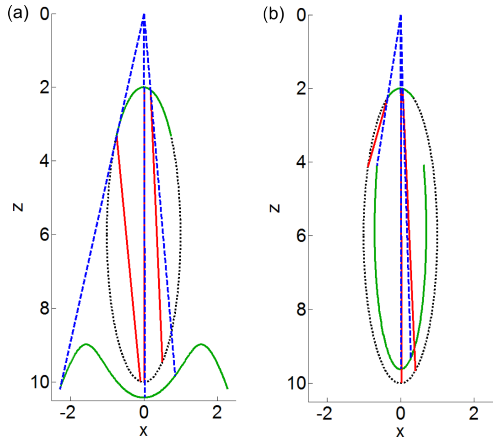

Figure 6. Curved array images (solid green line) of an elongated elliptical object (dotted black line) with $b = 1$ and $c = 4$ ($d + d_0 = 2$). Shown are the results for (a) $v_2 = 0.95v_1$ and (b) $v_2 = 1.05v_1$.

We first consider an elliptical object that is elongated along z, with nominal parameters $b = 1$ and $c = 4$. The image distortion, presented in figure 6 for both (a) $v_2 = 0.95v_1$ and (b) $v_2 = 1.05v_1$, shows similar qualitative structure for the circular object [figure 4] but with enhanced distortion. For $v_2 < v_1$, the flicks are even more pronounced than for the circular case, caused by the fast roll-off of the object boundary with x (which causes the angle of incidence to increase more quickly with x). The area distortions are $A_\mathrm{i}/A_\mathrm{r} = 1.58$ (for $v_2 < v_1$) and 0.68 (for $v_2/v_1 > 1$); this is vastly greater than for circular objects in Section 4.2, demonstrating the sensitive role of elongation.

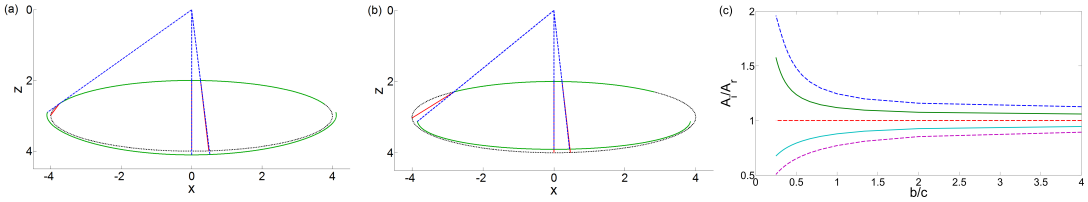

Figure 7. (a)-(b) Same as figure 6 but for a flattened elliptical object with $b = 4$ and $c = 1$. (c) Area distortion $A_\mathrm{i}/A_\mathrm{r}$ versus ellipticity b/c (with b fixed to unity) under curved array imaging. Various values of v_2/v_1 are considered ranging from 0.9 (top line) to 1.1 (lowest line) in steps of 0.05.

In contrast, for a flattened ellipse [figure 7 (a)-(b), nominal parameters $b = 4$ and $c = 1$] the image distortion is reduced, with negligible flicks appearing in the image due to the slower roll-off of the boundary with x. Also, the narrowness of the object in z means that the rays have little distance to accumulate any significant distortion. The area distortions here are $A_\mathrm{i}/A_\mathrm{r} = 1.06$ (for $v_2/v_1 < 1$) and 0.95 (for $v_2/v_1 > 1$), confirming the reduced distortion for flattened objects.

To further quantify the dependence on elongation, figure 7 (c) plots the area distortion $A_\mathrm{i}/A_\mathrm{r}$ as a function of ellipticity b/c. We clearly see that the distortion diverges for objects which are increasingly elongated (along z), and converges towards the undistorted result for increasingly flattened geometries.

We have compared the ray model predictions against experimental images of an elliptical object. These results, presented in Appendix B, further support the validity of the ray model in modelling the distortion of the boundary in the image.

6. Discussion and Conclusions

We have developed a ray model that describes the geometric distortion of two-dimensional ultrasound images (based on linear, curved, phased or vector arrays) of circular and elliptical objects due to speed of sound discrepancies. The geometric distortion arises from the refraction of the sound and the misrepresentation of length within the object. By comparing to ultrasound images of a test object we have validated that the ray model successfully captures the underlying geometric distortion of the image.

The geometric distortion of ultrasound images of circular objects has been examined previously [15, 16], including by ray models [14, 13]. Our analysis extends this previous body of work by *quantifying* the distortion of area, and thereby providing new insight into the errors in the ultrasonic evaluation of area and volume of anatomical features. Our work also extends previous analyses by considering elliptical objects, which allows us to explore the role of elongation, and by covering all four of the main transducers array formats.

When $v_2 < v_1$, the image is larger than the object, and vice versa for $v_2 > v_1$. The ray model predicts the emergence of gaps in the image boundary, an effect which may contribute to the phenomenon of acoustic shadowing [14, 15, 16, 13]. For $v_2 < v_1$ the image also features distinctive flicks at the extreme angular positions, as noted previously [14]. The deviation of the image area from the true value is greater for the "angled" array systems (phased, curved and vector arrays) than the linear array, due to the enhanced role of refraction. The deviation also depends on the shape and size of the object, in general increasing with the lateral size of the object and its elongation along the ultrasound axis.

In Ref. [16] it is argued that the true dimension of the object, along the axis of the interrogating beam, is the sonographic dimension of the object multiplied by the ratio of the object speed of sound to the scanner-assumed speed of sound (v_2/v_1 in our notation). In other words, the true object shape should correspond to the image shape scaled axially by a factor

v_2/v_1. From this it follows that the true and image areas are related by $A_\mathrm{r}/A_\mathrm{i} = v_2/v_1$. This linear relationship is shown in figure 8 (red line). However, we typically find the distortion to be considerably larger than this prediction, a difference which is then clearly attributable to refraction (not included in this result from Ref. [16]). To illustrate this, we have superimposed onto this figure our results (same parameters as figure 3) for a circular object based on a linear (green line) and curved array (blue line). It is evident that the Ziskin prediction underestimates the distortion, typically by a factor of 2-3 for these examples (more generally this factor will depend on the object shape, size and distance from the transducer). For example, for $v_2/v_1 = 1.05$, the ray model predicts $A_\mathrm{r}/A_\mathrm{i} = 1.1$ for a linear array and 1.16 for a curved array (c.f. 1.05 according to [16]). The area distortion has contributions from refraction of the rays at the near surface and the miscalculation of the length of the ray within the object. We can artificially remove the effect of refraction from the ray model by setting $\theta_\mathrm{r} = \theta_\mathrm{i}$. In doing so we find for a circular object that these effects roughly contribute to of the order of half of the area distortion (although, again, this will depend in general on the object parameters and shape).

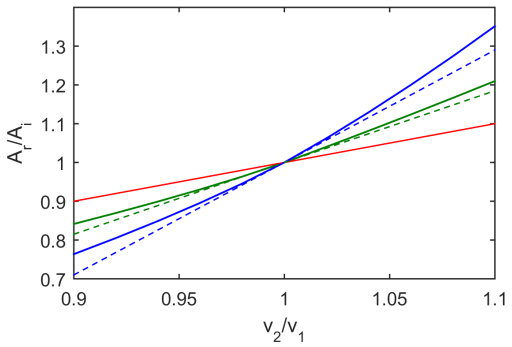

Figure 8. Ratio of the true object area to the image area, $A_\mathrm{r}/A_\mathrm{i}$, versus the speed ratio v_2/v_1. The ray model predictions for a circular object imaged via linear and curved array are shown by green and blue lines, respectively (the model parameters are as in figure 3). The prediction $A_\mathrm{r}/A_\mathrm{i} = v_2/v_1$, derived from Ref. [16], is shown by the red line. As a guide to the eye, straight lines with gradient 1.85 and 2.9 are shown by the dashed lines.

In its conventional clinical use, ultrasound provides qualitative, diagnostic images within the body. Increasingly, however, medical ultrasound is being pursued to provide *quantitative* volumetric measurements of organs and tumours [20, 21, 22]. This functionality allows, for example, the precise mapping of tumour growth and the efficacy of therapies, as well as the non-invasive measurement of urine volume in the bladder (negating the need for conventional cathetization techniques, which are uncomfortable and present an infection risk). Following improvements in 3D reconstruction of ultrasound images [34], ultrasound-based volume measurements are claiming to have errors of only a few percent across a variety of anatomical structures [26, 22, 29, 28]. These measurements do not take into account the effects of variable speed of sound which will geometrically distort the image and lead to systematic errors in the volume measurement. With 3D reconstructed images typically being formed from 2D images, the problem is essentially a 2D one. As such, these geometric distortions we examine here pose a key limiting factor on the current possible accuracy of these measurements. We hope to examine the 3D distortions in future work. Moreover, developments in this direction could lead to algorithms to correct the distortion in clinical measurements, allowing area and volume measurements which overcome the distortion limit.

Appendix A. Ray Model for $v_1 \neq v_0$

For simplicity our main ray model considered the ambient speed of sound v_1 to be matched to that of the scanner v_0, thereby negating the misrepresentation of distance as the ray travels through the ambient liquid. Here we extend the ray model to account for $v_1 \neq v_0$ with a curved array.

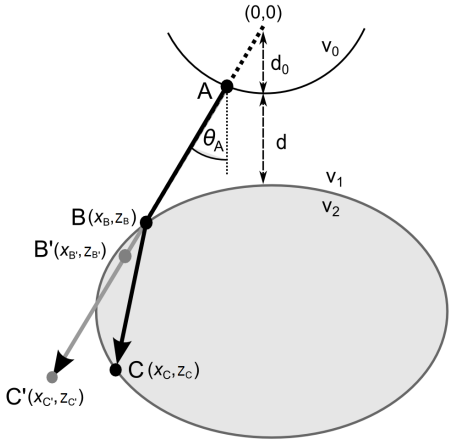

Figure A1. Schematic of the transducer-object scenario, featuring an elliptical object (speed of sound v_2) within an ambient medium (speed of sound v_1). The transducer is calibrated to a speed of sound v_0.

We consider a transducer element on the surface of the curved array, point A [figure A1]. Since the ray is emitted *normal* to the surface, no refraction effects occur at the transducer boundary, despite $v_1 \neq v_0$. The path of the real ray, which refracts into the object at point B on the near face and reaches the far boundary at point C, is provided by the same theory as before. The difference, however, now arises in the position of point B and its image point B'. We add a misregistration to all of the points by introducing the two relations for the misplacement of x and z, namely:

$$\Delta X = \left(\frac{v_0}{v_1} - 1\right)\left[\sqrt{x^2 + z^2} - d_0\right]\sin\theta_{\mathrm{A}},$$
$$\Delta Z = \left(\frac{v_0}{v_1} - 1\right)\left[\sqrt{x^2 + z^2} - d_0\right]\cos\theta_{\mathrm{A}},$$

which are similar to those in Ref. [36]. Thus the position of the image point B' is

$$(x_{\mathrm{B}'}, z_{\mathrm{B}'}) \quad = \quad (x_{\mathrm{B}} + \Delta X, z_{\mathrm{B}} + \Delta Z).$$

The total length of the virtual ray, the equivalent of equation (8), is

$$L_{\mathrm{AC}'} = \frac{v_0}{v_1} L_{\mathrm{AB}} + \frac{v_0}{v_2} L_{\mathrm{BC}},$$

and the image point C' is located at

$$(x_{\mathrm{C}'}, z_{\mathrm{C}'}) = (L_{\mathrm{AC}'}\sin\theta_{\mathrm{A}}, L_{\mathrm{AC}'}\cos\theta_{\mathrm{A}}).$$

Thus the distortion of the near-face and the far-face is completely determined.

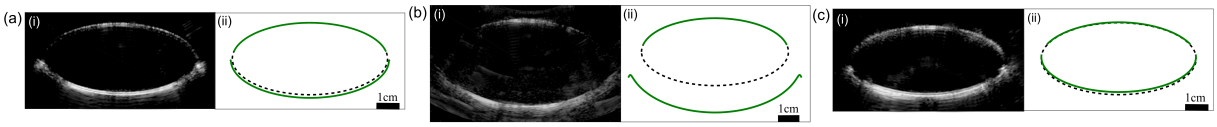

Figure B1. (i) B-mode images of the elliptical 2D object with $b/c \approx 1.9$ for various speed of sound combinations, with (ii) the corresponding ray model prediction of the image boundary (green lines). In (ii) the object boundary is also shown (black dashed line). (a) $v_2 = 1490$ m s^{-1} and $v_1 = 1540$ m s^{-1}, giving $v_2/v_1 = 0.968$. (b) $v_2 = 1100$ m s^{-1} and $v_1 = 1540$ m s^{-1}, giving $v_2/v_1 = 0.71$. (c) $v_1 = 1490$ m s^{-1} and $v_2 = 1540$ m s^{-1}, giving $v_2/v_1 = 1.034$.

Appendix B. Experimental images of elliptical objects and comparison to the ray model

As well as comparing against experimental images of a circular object, presented in Section 4.3, we have further compared against images of elliptical geometry. We repeat the methodology described in Section 3 using a hollow ellipsoidal shell. The shell is made of acrylic plastic, 1.5 mm thick. The shell is oblate (flattened along its axis of rotational symmetry), with external dimensions 31.8 mm (short diameter)) by 69.4 mm (long diameter). When the axis is aligned vertically and imaged directly from above, the imaged cross-section is a flattened ellipse with $b/c \approx 1.9$; when the axis is aligned horizontally, the imaged cross-section is an elongated ellipse with $b/c \approx 0.5$. The images for these two shapes for the three speed of sound cases (detailed in Section 3) are shown in Fig. B1 and Fig. B2, respectively.

The image boundary is of lower contrast and less sharp than for the circular object (Fig. 5), due to two differences. Firstly, the acoustic impedance of acrylic (≈ 3.3 MRayl) is approximately 5 times less than that of aluminium (≈ 17 MRayl) [41], giving a reduced reflectivity from the elliptical object. Secondly, the thicker shell of the elliptical object leads to less sharp boundary and some occurrences of reverberation echoes (see, e.g. the lower face of Fig. B1(c)(i)).

For the flattened case (Fig. B1) the distortion is evident for all three speed of sound scenarios, that is, the shift of the far face, the discontinuity in the image towards the equator of the object, and the distortion from an elliptical shape. This departure is particularly large for the case $v_2 \ll v_1$ (Fig. B1(b)), where the far face is appears at significantly increased depth, and the far face is stretched transversely by refractive effects, in good agreement with the prediction of the ray model. For three speed of sound cases (a-c), the model predicts $A_\mathrm{i}/A_\mathrm{r} = 1.076$, 1.63 and 0.98, which are close to the scanner estimates of $A_\mathrm{i}/A_\mathrm{r} = 1.05, 1.55$ and 0.97.

For the elongated case (Fig. B2), the image quality of the far (lower) face is further reduced. This is primarily due to the prominence of oblique rays (incident close to the object equator where the boundary is approximately vertical) which spend considerable time in the shell, introducing artefacts due to propagation through the shell itself (not accounted for within the model). To a lesser extent, the image quality of the far face is also reduced due to its relatively large distance from the transducer. Nonetheless, there is some qualitative agreement with the ray model, including the vastly shifted and stretched lower face for case (b) and the "squashing" of the lower face in case (c).

References

[1] Rumack C, Wilson S, Charboneau J and Levine D 2011 *Diagnostic Ultrasound 4th Edition* (Elsevier Mosby, Philadelphia)
[2] Fontanarosa D, Pesente S, Pascoli F, Ermacora D, Rumeileh I A and Verhaegen F 2013 *Phys. Med. Biol.* **58** 1341
[3] Duck F 2012, *Physical Properties of Tissue* (Institute of Physics and Engineering in Medicine, York)
[4] O'Donnell M and Flax S W 1988 *Ultrason. Imaging* **10** 1
[5] Anderson M E, McKeag M S and Trahey G E 2000 *J. Acoust. Soc. Am.* **107** 3540

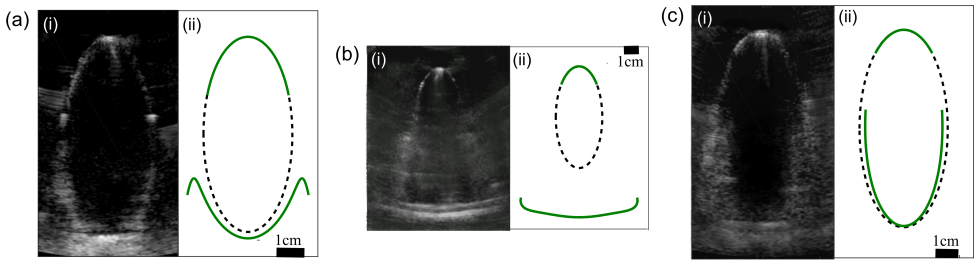

Figure B2. As Fig. B1 but when the object is rotated by 90°, realizing a 2D elliptical object with $b/c \approx 0.5$.

[6] T L Szabo 2004 *Diagnostic Ultrasound Imaging: Inside Out* (Elsevier, London)
[7] Napolitano D, Chou C-H, McLaughlin G, Ji T-L, Mo L, DeBusschere D and Steins R 2006 *Ultrasonics* **44** e43
[8] Cho M H, Kang L H, Kim J S and Lee S Y 2009 *Ultrasonics* **49** 774
[9] Shin H-C, Prager R, Gomersall H, Kingsbury N, Treece G and Gee A 2010 *Ultrasonics* **50** 716
[10] Yoon C, Lee Y, Chang J H, Song T and Yoo Y 2011 *Ultrasonics* **51**, 795
[11] Jaeger M, Robinson E, Akarcay H G and Frenz M 2015 *Phys. Med. Biol.* **60** 4497
[12] Robinson D E, Kossof G and Garrett W J 1966 *Ultrasonics* **4** 186
[13] Sommer F, Filly R and Minton M 1979 *Am. J. Roentgenol.* **132** 973
[14] Robinson D, Wilson L, Kossoff G 1981 *J. Clin. Ultrasound* **9** 181
[15] LaFollette P and Ziskin M 1986 *Ultrasound Med. Biol.* **12** 953
[16] Ziskin M, LaFollette P, Blathras K and V Abraham 1990 *Ultrasound Med. Biol.* **1** 183
[17] Opielinski K J and Gudra T 2000 *Ultrasonics* **38** 424
[18] Rubin J, Adler R, Fowlkes J and Carson P 1991 *Ultrasound Med. Biol.* **17** 85
[19] Steel R, Poepping T, Thompson R and Macaskill C 2004 *Ultrasound Med. Biol.* **30** 1153
[20] Campani R, Bottinelli O, Calliada F and Coscia D 1998 *Eur. J. Rad.* **27** S183
[21] Gilja O H, Hausken T, Berstad A and Odegaard, S 1999 *Proc. Instn Mech. Eng. H.* **213** 247
[22] Treece G, Prager R, Gee A and Berman L 2001 *Med. Im. Anal.* **5** 41
[23] Fontanarosa D, van der Meer S, Harris E and Verhaegen F 2011 *Medical Physics* **38** 2665
[24] Riccabona M, Nelson T and Pretorius D 1996 *Ultrasound Obstet. Gynecol.* **7** 429
[25] Riccabona M, Nelson T and Pretorius D 1996 *J. Ultrasound Med.* **15** 627
[26] Kristiansen N, Djurhuus J and Nygaard H 2004 *Med. Biol. Eng. Comput.* **42** 762
[27] Suwanrath C, Suntharasaj T and Sirapatanapipat H 2009 *J. Ultrasound Med.* **28** 847
[28] Tong S, Downey D B, Cardinal H N and Fenster A 1996 *Ultrasound Med. Biol.* **22** 735
[29] Huang Q H, Zheng Y P, Lu M H and Chi Z R 2005 *Ultrasonics* **43** 153
[30] Yoshizaki C T, Francisco R P V, de Pinho J C, Ruano R and Zugaib M 2013 *J. Ultrasound Med.* **32** 421
[31] Lyshchik A, Drozd V, Schloegl S and Reiners C 2004 *J. Ultrasound Med.* **23** 247
[32] Hornblower V D M, Yu E, Fenster A, Battista J J and Malthaner R A 2007 *Phys. Med. Biol.* **52** 91
[33] Linney A D and Deng J 1999 *Proc. Instn Mech. Eng. H.* **213** 235
[34] Fenster A, Downey D B and Cardinal H N 2001 *Phys. Med. Biol.* **46** R67
[35] Betrouni N, Lopes R, Makni N, Dewalle A S, Vermandel M and Rousseau J 2009 *Ultrasonics* **49** 646
[36] Goldstein A 2000 *Ultrasound Med. Biol.* **26** 1133
[37] Stewart J 2012 *Calculus 7th Edition* (Brooks/Cole, Belmont, USA)
[38] Bilaniuk N and Wong G 1993 *J. Acoust. Soc. Am.* **93** 1609-1612
[39] Benson G 1979 *J. Chem. Thermodyn.* **11** 861
[40] Tong J, Povey M, Zou X, Ward B and Oates C 2011 *J. Phys: Conf. Ser.* **279** 012023
[41] *Tables of Physical and Chemical Constants* (16th edition 1995). Kaye and Laby Online (www.kayelaby.npl.co.uk). Version 1.0 (2005)